IOP Publishing and International Atomic Energy Agency Nuclear Fusion
Nucl. Fusion **53** (2013) 113029 (9pp) doi:10.1088/0029-5515/53/11/113029

Measurements and simulations of low-wavenumber pedestal turbulence in the National Spherical Torus Experiment

D.R. Smith[1], S.E. Parker[2], W. Wan[2], Y. Chen[2], A. Diallo[3], B.D. Dudson[4], R.J. Fonck[1], W. Guttenfelder[3], G.R. McKee[1], S.M. Kaye[3], D.S. Thompson[1], R.E. Bell[3], B.P. LeBlanc[3] and M. Podesta[3]

[1] Department of Engineering Physics, University of Wisconsin-Madison, Madison, WI 53706, USA
[2] Department of Physics, University of Colorado, Boulder, CO 80309, USA
[3] Princeton Plasma Physics Laboratory, Princeton, NJ 08543, USA
[4] Department of Physics, University of York, Heslington, York YO10 5DD, UK

E-mail: drsmith@engr.wisc.edu

Received 9 May 2013, accepted for publication 7 October 2013
Published 24 October 2013
Online at stacks.iop.org/NF/53/113029

Abstract
Previous pedestal turbulence measurements in the National Spherical Torus Experiment assessed the spatial and temporal properties of turbulence in the steep gradient region of H-mode pedestals during edge localized mode (ELM)-free, MHD-quiescent periods. Here, we extend the analysis to fluctuation amplitudes and compare observations to pedestal turbulence simulations. Measurements indicate normalized fluctuation amplitudes are about 1–5% in the steep gradient region. Regression analysis indicates fluctuation amplitudes scale positively with electron density gradient, collisionality, and poloidal beta, and scale negatively with magnetic shear, electron density, ion temperature gradient (ITG), toroidal flow and radial electric field. The scalings are most consistent with trapped electron mode, kinetic ballooning mode, or microtearing instabilities, but, notably, least consistent with ITG turbulence. Gyrokinetic simulations of pedestal turbulence with realistic pedestal profiles show collisional instabilities with growth rates that increase at higher density gradient and decrease at higher ITG, in qualitative agreement with observed scalings. Finally, Braginskii fluid simulations of pedestal turbulence do not reproduce scalings from measurements and gyrokinetic simulations, and suggest electron dynamics can be a critical factor for accurate pedestal turbulence simulations.

(Some figures may appear in colour only in the online journal)

1. Introduction

Accurate models of the H-mode pedestal can enhance confidence in global confinement and first-wall heat load predictions for next-step devices. The pedestal region is notable for steep pressure gradients, high bootstrap current, and strong $E \times B$ shear. Global confinement is found to scale with pedestal height [1], and the pedestal can eject edge localized modes (ELMs) that degrade plasma performance and damage plasma-facing components. ELMs are attributed to peeling–ballooning and kinetic ballooning instabilities driven by pressure and current density gradients in the pedestal [2, 3]. In ELM-free scenarios, turbulence and micro-instabilities are likely important elements of pedestal dynamics and, therefore, global confinement. The spherical torus (ST) [4] edge region is among the most difficult regimes for plasma turbulence simulations due to the inherent challenges of edge simulations and the challenging ST parameter regime with high β ($2\mu p/B^2$), large ρ^* (ρ_s/a), strong beam-driven flow, and strong shaping. Simulations in large ρ^* regimes are challenging because ρ can be comparable to the pedestal width and gradient scale lengths, and the simulation domain exhibits significant shape variation. Pedestal stability calculations suggest ST plasmas can access higher pedestal gradients and heights than conventional aspect ratio tokamaks [5]. Past results from the National Spherical Torus Experiment (NSTX) [6] highlight the novel turbulence and transport properties of ST plasmas. For instance, stabilization or suppression of low-wavenumber (low-k) turbulence by strong equilibrium $E \times B$ flow shear [7] and field line curvature

[8] are leading explanations for near-neoclassical ion thermal transport in NSTX beam-heated plasmas [9, 10]. However, particle, momentum, and electron thermal transport remain anomalous and point to a turbulent transport mechanism. Recent linear and nonlinear gyrokinetic simulations in the NSTX core region point to a hybrid trapped electron mode (TEM)-kinetic ballooning mode (KBM) instability [11]. Also, the high β regime makes ST plasmas more susceptible to low-k microtearing (MT) modes [12–14], and the scaling of NSTX confinement time with collisionality is consistent with predictions from nonlinear MT mode simulations [15, 16]. Turbulence measurements at the top of the H-mode pedestal during the ELM cycle are found to be consistent with ion-scale turbulence [17], and recent linear gyrokinetic simulations in local, flux-tube geometry in the pedestal region identified hybrid TEM/KBM instabilities [18, 19]. On the Mega Amp Spherical Torus (MAST), beam emission spectroscopy measurements in the core region identified a critical balance among several turbulence timescales including correlation time, drift time, streaming time, and magnetic drift time [20, 21]. In addition, the longer turbulence decorrelation time is consistent with turbulence regulation by zonal flows.

Recent measurements of NSTX H-mode pedestal turbulence in the steep gradient region found poloidal correlation lengths $L_p/\rho_i \sim 10$, poloidal wavenumbers $k_\theta \rho_i \sim 0.2$, and decorrelation times $\tau_d/(a/c_s) \sim 5$ [22]. The normalized turbulence parameters are similar to those found in conventional tokamak pedestals [23]. Empirical scalings among turbulence quantities and local transport-relevant plasma parameters [24] were identified with regression analysis and model aggregation. For instance, the analysis identified positive L_p scalings for ∇n_e and collisionality and negative L_p scalings for ∇T_i. Collectively, the observed scalings in [22] are most consistent with transport driven by TEM, KBM, or MT turbulence, and least consistent with ion temperature gradient (ITG) turbulence.

Here, we extend the analysis in [22] to pedestal turbulence fluctuation amplitudes ($\tilde{n}/n$), and we compare observed scalings to fluid and gyrokinetic pedestal turbulence simulations with realistic pedestal profiles. Beam emission spectroscopy (BES) measurements at $r/a \approx 0.85$–0.95 in the steep gradient region show fluctuation amplitudes are $\tilde{n}/n \approx 1\% - 5\%$. Regression analysis and model aggregation identify positive $\tilde{n}/n$ scalings for $1/L_{ne}$, ν_i^*, and β_p and negative scalings for $\hat{s}$, n_e, ∇T_i, V_t and E_r. Building on [22], the $\tilde{n}/n$ scalings highlight the important role of density gradient, collisionality and β in pedestal turbulence. The $\tilde{n}/n$ scalings are partially consistent with TEM, KBM or MT instabilities, but, notably, least consistent with strongly driven ITG turbulence. The $\tilde{n}/n$ values from BES measurements are in good agreement with recent reflectometry measurements and modelling that show $\tilde{n}/n \lesssim 5\%$ in the pedestal [17], and $\tilde{n}/n$ scalings are consistent with results in [22]. `GEM` gyrokinetic simulations [25, 26] with realistic pedestal profiles indicate low-n instabilities (toroidal mode number; $6 \leqslant n \leqslant 10$) are electromagnetic, destabilized by collisions, and exhibit mixed-parity mode structure. Growth rates increase at higher ∇n_e and decrease at higher ∇T_i in qualitative agreement with observed scalings and in conflict with expected scalings for strongly driven ITG turbulence. Also, Braginskii fluid simulations using `BOUT++` [27, 28] highlight the importance of electron dynamics for accurate pedestal turbulence simulations. Section 2 describes BES measurements of pedestal turbulence in NSTX. Section 3 tabulates $\tilde{n}/n$ observations in the steep gradient region and identifies parametric scalings with transport-relevant plasma parameters. Next, section 4 compares measurements and scalings to gyrokinetic and fluid simulations of pedestal turbulence with realistic pedestal profiles. Finally, section 5 gives a summary of results.

2. Pedestal turbulence measurements with BES

The BES system on NSTX [29, 30] measures D_α emission ($n = 3 \rightarrow 2$, $\lambda_0 = 656.1$ nm) from deuterium heating beams to observe ion gyroscale fluctuations associated with low-k turbulence and instabilities. BES measurements are sensitive to plasma density fluctuations with

$$\frac{\tilde{n}}{\langle n \rangle_{dc}} = C \frac{\tilde{I}_{D\alpha}}{\langle I_{D\alpha} \rangle_{dc}} \quad (1)$$

where $I_{D\alpha}$ is the beam D_α emission intensity, n is the plasma density, and $\langle \cdots \rangle_{dc}$ is the dc time average [31]. The coefficient $C = C(E_{NB}, n, T_e, Z_{eff}) \approx 2.14$–$2.34$ is obtained from atomic calculations for typical values at the $R = 140$ cm location in figure 1 and table 1 [32, 33]. In the analysis below, we use the midpoint value $C = 2.24$. The BES channel layout on NSTX provides core-to-SOL radial coverage and four discrete poloidal arrays [29, 30]. In particular, the poloidal array at $R = 140$ cm and $r/a \approx 0.85$ is well positioned for pedestal turbulence measurements, as shown in figure 1. BES measurements on NSTX are sensitive to fluctuations with $k_\perp \rho_s \lesssim 1.5$ where $\rho_s \approx 0.5$–1.5 cm is the ion sound gyroradius (T_e, $T_i \approx 0.3$–1.0 keV) with spatial localization is $\Delta R \approx \Delta Z \approx 2.5$ cm. Previous point spread function (PSF) calculations with atomic excited state lifetimes for NSTX BES measurements indicate image distortion in the pedestal region is generally mild with radial smearing around 15% [30], so PSF corrections are not applied to the analysis below.

ELM-free, MHD-quiescent periods in H-mode discharges were identified in [22] to investigate low-k pedestal turbulence in NSTX ($k_\theta \rho_i \sim 0.2$ and $0.8 < r/a < 0.95$). The data set in [22] is reused here for further analysis. BES signals are frequency filtered to isolate 8–50 kHz components, the typical frequency range for observed broadband turbulence. ELM-free, MHD-quiescent periods lasting at least 200 ms were identified in discharges with $B_{T0} = 4.5$ kG, $I_p = 700$–900 kA, and lower single-null geometry. Plasma parameters slowly evolve during long ELM-free, MHD-quiescent periods, so the periods are partitioned into 15–45 ms data windows for measurement averaging. In total, 129 data windows were identified in 29 discharges. Figure 1 shows a subset of plasma profiles in the database. Multi-point Thomson scattering provides electron density and temperature (n_e and T_e) measurements [34], and charge exchange spectroscopy provides ion temperature and toroidal velocity measurements (T_i and V_t) [35]. Radial electric field (E_r) profiles are inferred from carbon density, temperature, and toroidal velocity. The poloidal velocity contribution to E_r is neglected because past

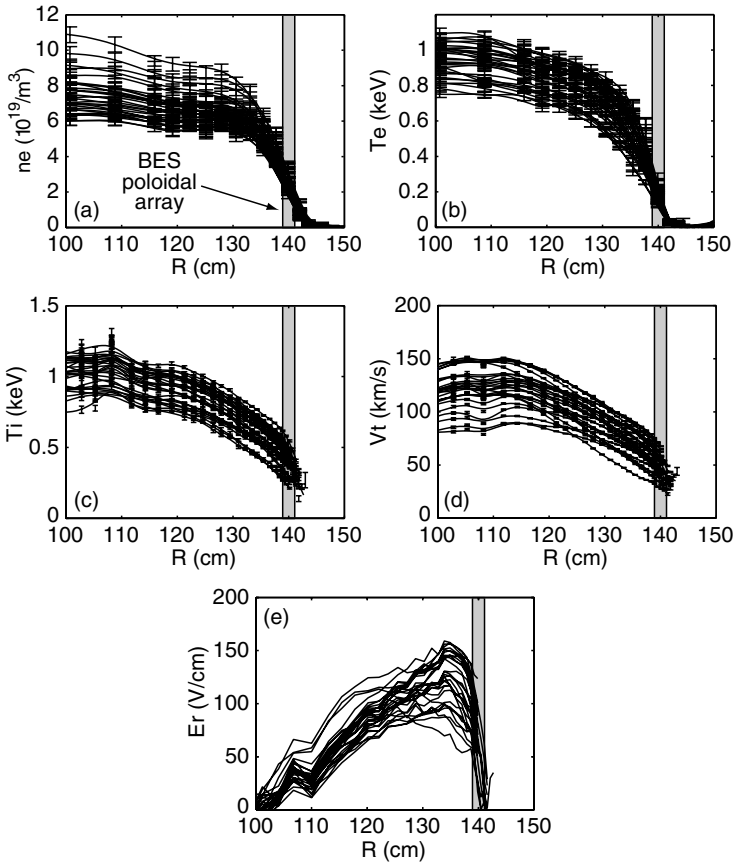

Figure 1. A subset of plasma profiles in a database for ELM-free, MHD-quiescent phases in H-mode plasmas. The grey box denotes the BES poloidal array at $R = 140$ cm.

measurements on NSTX and MAST suggest the poloidal velocity contribution is small even in the strong gradient region of the H-mode pedestal [20, 36, 37]. Incidentally, E_r shear quantities are omitted from the analysis due to large uncertainties associated with the second derivative of the measured T_i profile. In [22], pedestal turbulence measurements in the steep gradient region showed poloidal correlation lengths $L_p/\rho_i \sim 10$, poloidal wavenumbers $k_\theta \rho_i \sim 0.2$, and decorrelation times $\tau_d/(a/c_s) \sim 5$. Table 1 lists 10th–90th percentile ranges for turbulence quantities and plasma parameters in the database. Plasma parameters generally show 50–300% variation, but inverse aspect ratio ϵ, elongation κ, lower triangularity δ_l, ρ_s^* and ρ_i^* show less variation. Low-variation parameters are problematic for regression analysis, and such parameters should be omitted from the analysis. The variation in low-variation parameters are likely dominated by random noise, such as measurement error or magnetic reconstruction uncertainties. Regression analysis with low-variation parameters leads to models with large uncertainties, low statistical significance, and inconsistent model coefficients. Low variation in ϵ, κ, and δ_l is possibly due to screening for ELM-free, MHD-quiescent H-mode discharges. In the analysis below, ϵ, κ, δ_l, ρ_s^*, and ρ_i^* are omitted from analysis due to low variation in the database.

Figure 2(*a*) shows an example BES power spectrum and noise contributions. In the measurement database, typical signal-to-noise ratios are $S/N = 40$–500 for the band 8–50 kHz. Noise contributions are removed from BES signals before calculating $\tilde{n}/n$ using equation (1). Next, beam-induced fluctuations at the measurement location can contaminate measurements with fluctuation artefacts from outboard locations, so it is important to assess beam-induced fluctuations. Beam-induced fluctuations arise from fluctuations in the neutral beam deposition at an upstream location with large plasma fluctuations. Here, we apply two techniques to assess beam-induced fluctuations. First, in figure 2(*b*), we assess coherence between the principle measurement location ($R = 140$ cm) and outboard (upstream) locations. Figure 2(*b*) shows high coherence with the radially adjacent channel at $R = 142$ cm, which is expected given the radial size of turbulent eddies. For $R \geqslant 144$ cm, the coherence is low and near the noise level (dashed line). Therefore, the coherence spectra in figure 2(*b*) indicate the location $R = 140$ cm is not susceptible to beam-induced fluctuations at outboard locations. Second, we assess coherence between a radially distant core location and locations spanning the pedestal. Core BES measurements are susceptible to beam-induced fluctuations that originate in the edge region, and inverted ($\pm\pi$) cross-phases between radially separated channels are an indication of beam-induced fluctuations. Here, BES measurements in the pedestal are not likely susceptible to beam-induced fluctuations, but we present the analysis for completeness. Figures 2(*c*) and (*d*) show example coherence and cross-phase spectra for BES radial channels spanning the pedestal at $R = 137$–146 cm. The spectra are calculated with respect to a reference channel closer

Table 1. Database quantities.

Parameter	Median (range[a])	Parameter	Median (range[a])
Turbulence quantities measured at $R = 140\,cm$			
$\tilde{n}/n$ (%)	2.1 (1.2–4.7)	$k_\theta\,\rho_i$	0.17 (0.074–0.31)
L_p/ρ_i	11 (7.5–18)	$\tau_d/(a/c_s)$	4.4 (2.6–7.6)
Local plasma parameters at $R = 140\,cm$			
n_e (10^{13} cm^{-3})	2.0 (1.7–2.5)	ρ_s^* (ρ_s/r)	0.019 (0.017–0.021)
$\lvert\nabla n_e\rvert$ (10^{13} cm^{-4})	0.68 (0.57–0.90)	ρ_i^* (ρ_i/r)	0.023 (0.021–0.025)
$1/L_{ne}$ (cm^{-1})[b]	0.34 (0.28–0.44)	δ_r^{sep} (cm)[f]	−0.68 (−0.77–−0.52)
T_e (keV)	0.15 (0.11–0.19)	q	7.1 (5.9–9.7)
$\lvert\nabla T_e\rvert$ (keV cm^{-1})	0.79 (0.061–0.093)	$\hat{s}$	3.3 (2.5–5.4)
$1/L_{Te}$ (cm^{-1})[b]	0.52 (0.47–0.64)	ϵ	0.59 (0.56–0.63)
T_i (keV)	0.42 (0.33–0.50)	κ	2.44 (2.36–2.51)
$\lvert\nabla T_i\rvert$ (keV cm^{-1})	0.064 (0.029–0.15)	δ_l	0.8 (0.61–0.73)
$1/L_{Ti}$ (cm^{-1})[b]	0.15 (0.07–0.33)	ν_{ee} (10^6 s^{-1})	0.58 (0.43–0.80)
V_t (km s^{-1})	55 (37–68)	ν_e^* ($\nu_{ee}\,qR/v_{th,e}$)	0.77 (0.51–1.5)
∇V_t (10^6 s^{-1})	0.89 (0.33–1.7)	ν_{ii} (10^3 s^{-1})	2.1 (1.5–3.4)
E_r (V cm^{-1})	68 (11–104)	ν_i^* ($\nu_{ii}\,qR/v_{th,i}$)	0.10 (0.071–0.21)
n_{ped} (10^{13} cm^{-3})[d]	6.8 (5.9–8.1)	β (%)[c]	3.9 (3.0–5.3)
ΔR_{ped} cm[d]	18 (15–21)	β_e (%)[c]	1.1 (0.69–1.6)
L_n/L_{Te}	1.6 (1.2–1.9)	β_p (%)[c]	10 (7.6–13)
L_n/L_{Ti}	0.41 (0.20–1.0)	r/a	0.91 (0.84–0.96)

[a] 10th–90th percentiles.
[b] $1/L_X \equiv \lvert\nabla X\rvert/X$.
[c] $\beta \equiv 2\mu_0\,(p_e + p_i)/B^2$, $\beta_e \equiv 2\mu_0\,p_e/B^2$ and $\beta_p \equiv 2\mu_0\,(p_e + p_i)/B_p^2$.
[d] Pedestal height n_{ped} and width ΔR_{ped} from electron density profile piece-wise fits to linear and tanh functions with continuous first derivative.
[e] Outboard radial distance to second separatrix.
[f] $\delta_r^{sep} < 0$ for lower single null configuration.

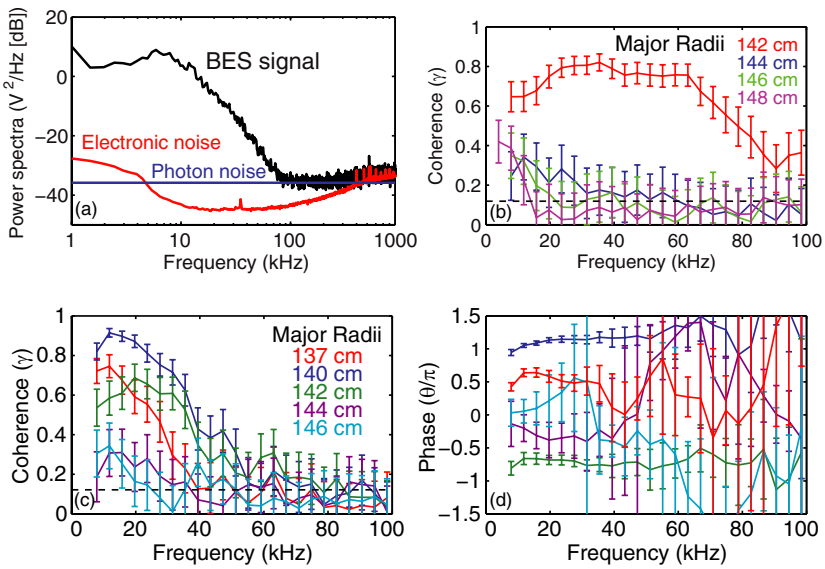

Figure 2. (*a*) Power spectra for BES signal, electronic noise, and photon noise. (*b*) Coherence spectra for radial channels outboard of the measurement location at $R = 140$ cm. (*c*) Coherence and (*d*) cross-phase spectra for radial channels spanning the pedestal relative to the core channel at $R = 129$ cm. The dashed line in (*b*) and (*c*) represents the coherence noise level.

to the core at $R = 129$ cm. The $R = 140$ cm measurement location shows the highest coherence level and nearly inverted cross-phase. In contrast, other channels show lower coherence, and cross-phases are not fully inverted. Figures 2(*b*)–(*d*) shows a single example, but the $R = 140$ cm location showed the largest coherence and inverted cross-phase for all measurements in the database. The measurements indicate fluctuations near $R = 140$ cm are the dominant contribution to beam-induced fluctuations in the core. The analysis below is derived from BES measurements at $R = 140$ cm, so we infer that the measurements are not susceptible to beam-induced fluctuations from locations at $R > 140$ cm.

In table 1, the 10th–90th percentile range for $\tilde{n}/n$ is 1.2–4.7% for the band 8–50 kHz, and figures 3(*a*) and (*b*) shows the distribution of $\tilde{n}/n$ values in the database. The $\tilde{n}/n$ values from BES pedestal measurements show good agreement with previous reflectometry pedestal measurements that showed $\tilde{n}/n \lesssim 5\%$ [17]. Atomic physics estimates give

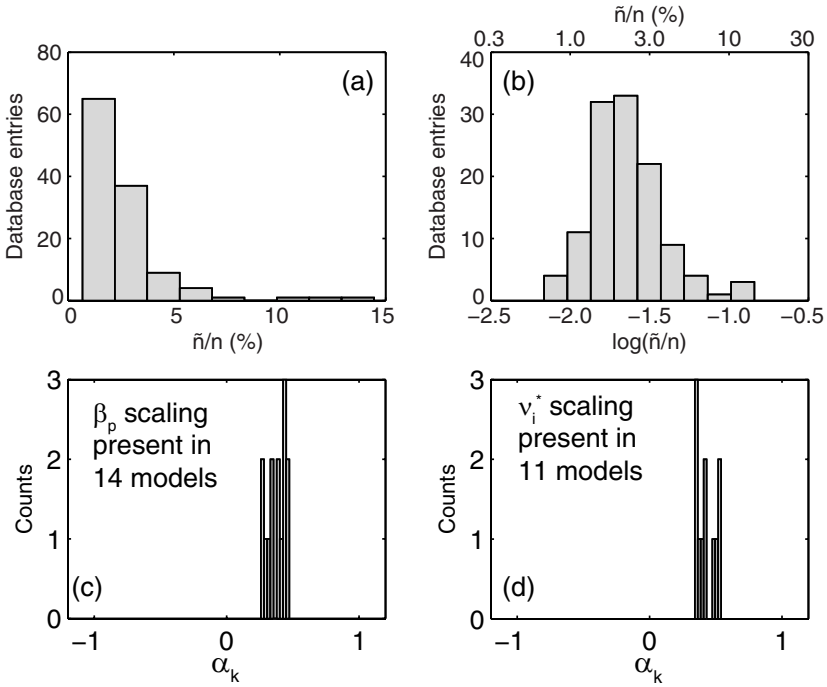

Figure 3. (*a*), (*b*) Histogram of $\delta n/n$ values from the database; (*c*) histogram of β_p and (*d*) ν_i^* scalings that emerge from model aggregation ($\alpha > 0$ indicates a positive scaling).

$\tilde{n}/n = 2.24\,\tilde{I}_{D\alpha}/I_{D\alpha} = 2.24\,\tilde{V}_{corr}/\langle V_{corr}\rangle_{dc}$ (see equation (1)) where $I_{D\alpha}$ is the neutral beam D_α emission intensity, $\tilde{V}_{corr}$ is the 8–50 kHz BES detector signal with photon noise and thermal noise corrections, and $\langle V_{corr}\rangle_{dc}$ is the detector dc signal with noise corrections [30]. Reference [22] identified parametric scalings among turbulence quantities (L_p, k_θ, τ_d) and transport-relevant plasma parameters. In the next section, we extend the analysis to parametric scalings between $\tilde{n}/n$ and plasma parameters.

3. Parametric scalings of pedestal turbulence fluctuation amplitudes

With a database of $\tilde{n}/n$ observations and local transport-relevant plasma parameters in hand, we now identify parametric dependencies using stepwise multivariate linear regression (SMLR) and model aggregation, an analysis technique described in [22]. This analysis implicitly presumes that local plasma parameters influence turbulence characteristics [24]. With y_i denoting a turbulence quantity and $x_{k,i}$ denoting local plasma parameters, the SMLR algorithm finds models in the form

$$\frac{\hat{y}_i - \bar{y}}{\sigma_y} = \sum_k \alpha_k \frac{x_{k,i} - \bar{x}_k}{\sigma_k}, \qquad (2)$$

where σ are standard deviations for y_i and $x_{k,i}$, and $\hat{y}_i$ are model predictions for turbulence quantities (i indexes database entry and k indexes plasma parameter). The dimensionless α_k parameters are linear scaling coefficients between y_i and $x_{k,i}$ when other parameters in the model are fixed; parameters absent from the model are unconstrained. The SMLR algorithm minimizes the model's squared sum of errors, $SSE \equiv \sum_i (\hat{y}_i - y_i)^2$, by adding or removing x_k parameters such that the inferred significance of each α_k value exceeds 95% [38]. Many statistically valid models (that is, SSE local minima) can exist in the high-dimensional x_k space. Identifying a 'best' model from a large group of valid models is unnecessarily restrictive, highly subjective, and susceptible to investigator bias. Therefore, we employ model aggregation to identify parametric scalings that are consistent across a variety of model scenarios. In short, model aggregation provides (1) more parametric scalings than a single model and (2) a distribution of scaling coefficients that cover a variety of model constraints. Model aggregation is conceptually similar to ensemble machine learning in which multiple viable models are combined into a single model. The virtues and capabilities of model aggregation and ensemble machine learning are documented in statistics [39, 40], economics [41–43], ecology [44], and genomics [45]. We seek to identify as many models as possible in the high-dimensional parameter space, so we initialize the SMLR algorithm with over 2000 initial models for every 2, 3 and 4 parameter combination. Finally, note that linear regression does not require or presuppose linearity in the true function relationship among parameters, and linear regression does not attempt to identify the true functional relationship among parameters. Instead, linear regression identifies the effective linear scaling (i.e. slope) among parameters with an unknown functional relationship. As in [22], models identified by the SMLR algorithm are screened for multicollinearity and residual normality to ensure the statistical properties are acceptable.

The SMLR algorithm fails to identify models in the form of equation (2) for the highly skewed $\tilde{n}/n$ distribution in figure 3(*a*), but the algorithm successfully identifies models using the transformed quantity $\log(\tilde{n}/n)$ shown in figure 3(*b*).

Table 2. 10th–90th percentiles for statistical characteristics of regression models.

Figure of merit	$\log(\tilde{n}/n)$ models
# models	27
R^2	0.51–0.57
max($\lvert C_{jk}\rvert$)	0.49–0.70
max(VIF$_k$)	1.7–6.3
max($\lvert r_i^s\rvert/t_{95}$)	0.74–0.90
$\lvert Sk\rvert/\sigma_{Sk}$	0.17–2.0
$\lvert Kt\rvert/\sigma_{Kt}$	0.05–1.3

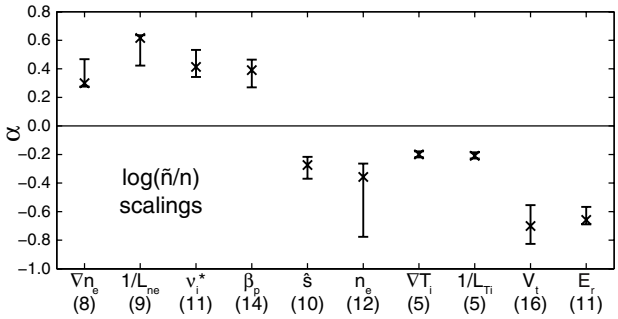

Figure 4. 10th–90th percentile ranges for scalings that emerge from model aggregation for $\log(\delta n/n)$. $\alpha > 0$ ($\alpha < 0$) denotes a positive (negative) scaling, and numbers below labels indicate the number of models that contain the scaling.

Specifically, in the following analysis, the quantity $y_i \equiv \log(\tilde{n}_i/n_i)$ is applied in equation (2). The SMLR algorithm was initialized with about 2600 parameter combinations, and the algorithm returned 27 unique models for $\log(\tilde{n}/n)$. Table 3 lists statistical metrics for the $\log(\tilde{n}/n)$ models. R^2 values indicate the models generally capture 50–60% of the variation in $\log(\tilde{n}/n)$ (coefficient of determination, or goodness of fit, $R^2 \equiv \sum(\hat{y}_i - \bar{y})^2/\sum(y_i - \bar{y})^2$). Maximum pairwise correlations (max($|C_{jk}|$)) and maximum variance inflation factors (max(VIF$_k$)) indicate the models are not susceptible to excessive uncertainty from correlations among regression variables (x_k). Incidentally, regression analysis does not require statistical independence among parameters, and functional relationships among parameters are permissible and not inherently problematic. Model uncertainties increase as parameters become linearly inter-dependent, and the VIF$_k$ metric quantifies the linearity. Finally, maximum studentized residuals (max($|r_i^s|/t_{95}$)), normalized skewness ($|Sk|/\sigma_{Sk}$), and normalized excess kurtosis ($|Kt|/\sigma_{Kt}$) indicate residual distributions are consistent with a random sample from a normal distribution—a necessary condition for statistically valid regression models (table 2).

Model aggregation identifies several parametric scalings for $\log(\tilde{n}/n)$ in the steep gradient region of the pedestal. For example, figures 3(*c*) and (*d*) show positive scalings ($\alpha > 0$) for β_p and ν_i^* from several models. Specifically, the scalings indicate $\log(\tilde{n}/n)$ increases at higher β_p and higher ν_i^*. Figure 4 shows additional scalings for $\log(\tilde{n}/n)$ including positive scalings for ∇n_e and $1/L_{ne}$ and negative scalings for $\hat{s}$, n_e, ∇T_i, $1/L_{Ti}$, V_t, and E_r. Additional scalings for ν_e, ν_e^*, and ν_i are consistent with ν_i^* scalings, but not shown in figure 4. Note that the analysis successfully identifies scalings with respect to some plasma parameters, such as ∇T_i, and fails to identify scalings for other plasma parameters, such as T_i. The failure to find a particular scaling has several possible interpretations including (1) the data fails to exhibit the scaling, (2) the scaling is weak ($\alpha \approx 0$), and (3) the scaling uncertainty is sufficiently large to compromise the entire regression model.

Positive scalings for $1/L_{ne}$ and ∇n_e in figure 4 point to an instability driven by density gradient, such as TEM [46, 47] or possibly KBM [48, 49] instabilities. Notably, positive scalings for density gradient and negative scalings for ITG are inconsistent with strongly driven ITG turbulence [50], like results in [22]. However, we note that fluctuation amplitudes for marginally stable ITG turbulence do not necessarily increase as the turbulent drive increases [51]. Positive scalings for collisionality are consistent with MT instabilities [16, 49], but not drift-wave turbulence like ITG or TEM. However, inferring meaning from collisionality scalings can be challenging due to collisional stabilization of turbulence and collisional damping of zonal flows that suppress turbulence. Also, positive scalings for poloidal β point to MT or KBM instabilities. Negative scalings for $\hat{s}$ are consistent with eddy distortion and turbulence reduction via magnetic shear. Negative scalings for n_e indicate $\tilde{n}/n$ increases at lower n_e, consistent with past measurements that show $\tilde{n}/n$ increases towards the edge. Finally, negative scalings for V_t and E_r suggests turbulence suppression by flow shear [52, 53] because V_t and E_r values in the pedestal are related to the associated gradient values (see figures 1(*d* and (*e*))).

The $\tilde{n}/n$ scalings described above and scalings from [22] point to TEM, KBM, or MT turbulence in the steep gradient region of NSTX H-mode pedestals during ELM-free, MHD-quiescent periods. To augment experimental scalings, we investigate gyrokinetic and fluid simulations of NSTX pedestal turbulence in the next section.

4. Simulations of pedestal turbulence

To complement observed scalings from section 3 and [22], we now turn to linear gyrokinetic simulations and nonlinear fluid simulations of pedestal turbulence. The simulations use realistic pedestal profiles from the database of turbulence measurements summarized in table 1. `GEM` is a δf particle-in-cell code with gyrokinetic ions and drift-kinetic electrons, but not neutral species [25, 26]. `GEM` simulations are electromagnetic, collisional, and global in the pedestal region with realistic profiles from figure 1 ($0.75 \lesssim r/a \lesssim 0.99$). Linear gyrokinetic simulations can be indicative of instabilities, but linear simulations may fail to identify nonlinear processes such as subcritical turbulence, nonlinear spreading, and the dominant nonlinear instability [54]. However, nonlinear gyrokinetic simulations of the ST pedestal region are not sufficiently tractable at this time. The `GEM` simulations give linear growth rates for instabilities at multiple toroidal modes in the range $n = 6$–18. Modes $6 \leqslant n \leqslant 10$ correspond to $k_\theta \rho_i \approx 0.2$, the typical observed wavenumbers in table 1. Note that pedestal profiles in `GEM` simulations are artificially flattened at the domain boundary to suppress boundary artefacts, and gyrokinetic ordering parameters in the steep gradient region are marginal with $\rho_i/L_{Ti} \approx 0.2$ and $\rho_i/L_{ne} \approx \rho_i/L_{Te} \approx 0.4$. Finally, we present

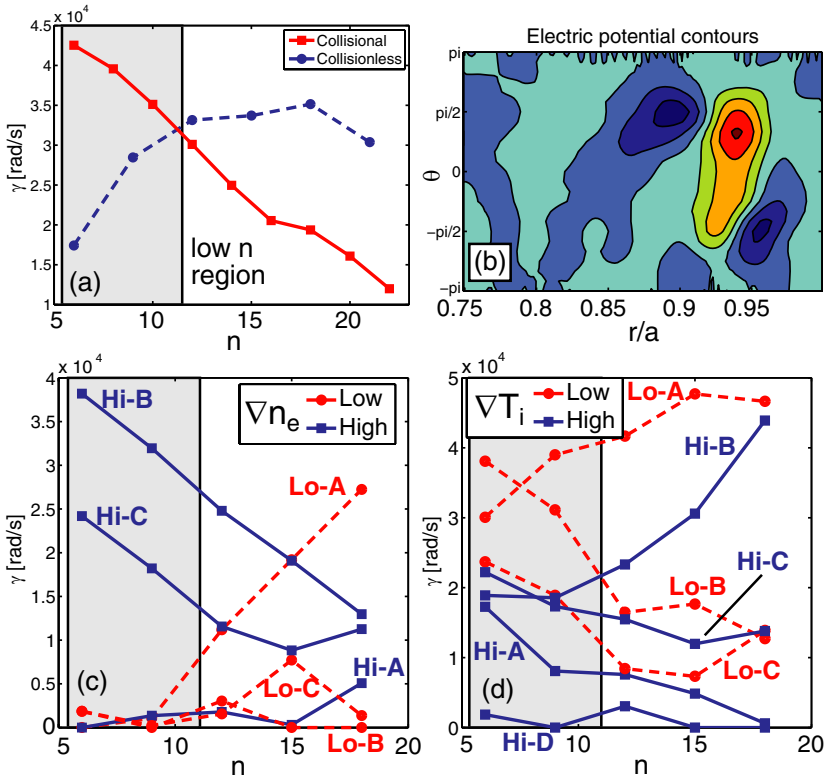

Figure 5. (*a*) Collisional and collisionless simulations with the low-*n* region in the grey box, (*b*) field-aligned electric potential contours, (*c*) high and low ∇n_e scenarios and (*d*) high and low ∇T_i scenarios. Simulation parameters at $R = 140$ cm are listed in table 3.

here linear GEM simulations, but nonlinear GEM simulations are in progress.

GEM pedestal simulations indicate low-*n* instabilities with $6 \leqslant n \leqslant 10$ (n is toroidal mode number) are destabilized by collisions and exhibit mixed-parity mode structures. The modes correspond to $k_\theta \rho_i = (nq/r)\rho_i \approx 0.2$, where q (safety factor), r (minor radius), and ρ_i are evaluated at the centre of the simulation domain. Collisional and collisionless simulations in figure 5(*a*) show the collisional destabilization of low n modes, or, in an alternate interpretation, collisions shift the most unstable mode to lower n. Collisional destabilization is consistent with the positive $\tilde{n}/n$ scaling for ν_i^* in figure 4 and the positive L_p scaling for ν in [22]. Also, the shift to lower n instabilities with collisions is consistent with smaller k_θ at higher ν in [22]. Next, figure 5(*b*) shows field-aligned electric potential contours for $n = 6$. The hybrid, or mixed parity, mode structure is not clearly ballooning parity or tearing parity. Though speculative, a hybrid TEM/MT instability could generate a hybrid mode structure and be consistent with several observed scalings in figure 4 and [22] including ∇n_e, ∇T_i, ν and β scalings. In addition, the global GEM simulations are consistent with recent local gyrokinetic simulations that indicate NSTX pedestals with and without lithium conditioning are susceptible to TEM, KBM and MT instabilities [18, 19].

GEM pedestal simulations for high and low ∇n_e and ∇T_i scenarios indicate low-*n* modes are destabilized at higher ∇n_e and stabilized at higher ∇T_i. The scenarios are selected from the database summarized in table 1 for ∇n_e and ∇T_i values larger or smaller than median values, but other plasma parameters are comparable to median values. Consequently, the scenarios are not akin to single-parameter scans often found in simulation investigations. Single-parameter scans can be insightful, but the scans are often unrealistic and lack self-consistency. Instead, the scenarios include some variation in plasma parameters, but the variation was minimized. Unlike parameter scans, simulations based on observed profiles are inherently self-consistent and realistic. Figure 5(*c*) shows GEM growth rates (γ) for several high and low ∇n_e scenarios from measured profiles in figure 1. Two of the three high ∇n_e scenarios exhibit large growth rates at low n, and all low ∇n_e scenarios exhibit low growth rates. The correlation between ∇n_e and growth rates in figure 5(*c*) is consistent with ∇n_e scalings for $\tilde{n}/n$ in figure 4. Also, in the framework of turbulent transport models ($D, \chi \sim L_p^2/\tau \sim \gamma/k^2$), higher growth rates at higher ∇n_e are consistent with observed scalings that show positive ∇n_e scalings for L_p in [22]. Next, figure 5(*d*) shows GEM growth rates for several ∇T_i scenarios from measured profiles. At low n, the high ∇T_i scenarios exhibit lower growth rates. Again, the correlation between ∇T_i and growth rates in figure 5(*d*) is consistent with ∇T_i scalings for $\tilde{n}/n$ in figure 4. Also, in the framework of turbulent transport models, smaller growth rates at higher ∇T_i are consistent with negative ∇T_i scalings for L_p in [22]. The ∇n_e and ∇T_i trends from GEM are consistent with observed $\tilde{n}/n$ scalings from figure 4 and L_p scalings from [22]. The consistency between GEM growth rates and observed scalings for ∇n_e and ∇T_i is an encouraging result, but conclusive identification of turbulent modes active in the pedestal and robust validation of pedestal models requires further analysis.

We also performed fluid simulations using BOUT++, a 3D initial value code with flexible implementation of fluid

Table 3. Measured plasma parameters at $R = 140$ cm for simulations in figure 5.

∇n_e Scenarios	$\lvert\nabla n_e\rvert$ (10^{13} cm^{-4})	L_n/L_{Ti}
Low-A	0.56	0.46
Low-B	0.60	0.51
Low-C	0.57	0.35
High-A	0.80	0.36
High-B	0.76	0.32
High-C	0.73	0.40
∇T_i Scenarios	$\lvert\nabla T_i\rvert$ (keV cm^{-1})	L_n/L_{Ti}
Low-A	0.037	0.33
Low-B	0.043	0.32
Low-C	0.046	0.40
High-A	0.13	0.82
High-B	0.095	0.82
High-C	0.078	0.46
High-D	0.083	0.51

plasma models [27, 28]. We apply a Braginskii fluid model from [28] that nonlinearly evolves n_i, ϖ (vorticity), ϕ, $j_\parallel$, $A_\parallel$, T_i and T_e, and the model includes collisions, $E \times B$ advection, field line curvature, and drive terms for $j_\parallel$ and ∇P. The fluid model does not include equilibrium toroidal rotation and ion parallel advection. Importantly, the model can not capture electron dynamics including trapped electron effects, so TEM and MT instabilities are not feasible with the fluid model. In addition, the radial electric field and $E \times B$ advection include only the pressure gradient term. Correlation lengths from BOUT++ simulations with profiles from figure 1 are $L_p/\rho_i \sim 8$, generally consistent with observations. However, ∇n_i and ∇T_i simulation scenarios showed higher $\tilde{n}_i/n_i$ saturation at low ∇n_i and high ∇T_i, trends opposite to observed $\tilde{n}/n$ scalings in figure 4. The $\tilde{n}_i/n_i$ trends are consistent with strongly driven ITG turbulence. A complete E_r with equilibrium toroidal rotation may have generated E_r shear sufficient to suppress ITG. However, the GEM gyrokinetic simulations also lacked equilibrium toroidal rotation, yet the simulations were least consistent with strongly driven ITG turbulence. To summarize, the BOUT++ simulations indicate pedestal turbulence simulations require either realistic electron dynamics or realistic E_r with equilibrium toroidal rotation. The GEM simulations, however, suggest electron dynamics, not toroidal rotation, is the key ingredient. As an aside, the BOUT++ simulations also indicate that simple, order-of-magnitude agreement between turbulence quantities, such as correlation length, can lead to erroneous inferences and underscores the importance of more sophisticated analysis. Finally, the recent implementation of a gyrofluid model with electron dynamics in BOUT++ will enable more realistic simulations of pedestal turbulence with TEM and MT instabilities in the future [55].

5. Summary

Confinement projections for ITER and next-step devices depend on accurate pedestal models, and the ST regime can expand the parameter space for model validation. Previous measurements of low-k turbulence in the steep gradient region of the NSTX H-mode pedestal during ELM-free, MHD quiescent periods showed broadband turbulence with poloidal correlation $L_p/\rho_i \sim 10$, poloidal wavenumber $k_\theta \rho_i \sim 0.2$, and decorrelation time $\tau_d/(a/c_s) \sim 5$ [22]. Further analysis showed positive L_p scalings for ∇n_e and ν and negative L_p scalings for ∇T_i. Here, we extended the analysis to $\tilde{n}/n$ scalings and performed gyrokinetic simulations with realistic pedestal profiles. $\tilde{n}/n$ measurements in the steep gradient region are about 1–5% for the band 8–50 kHz. Similar to L_p scalings, $\tilde{n}/n$ increases at higher ∇n_e, ν_i^*, and β_p, and $\tilde{n}/n$ decreases at higher $\hat{s}$, ∇T_i and E_r. Collectively, the scalings are partially consistent with TEM, KBM or microtearing instabilities, and, notably, inconsistent with the ITG instability.

Linear GEM gyrokinetic simulations with realistic pedestal profiles indicate low-n growth rates increase with collisionality, increase at higher ∇n_e, and decrease at higher ∇T_i. The GEM simulations are consistent with observed scalings and the inferred inactive or subdominant ITG turbulence. However, linear instabilities in GEM simulations are not necessarily representative of the observed turbulence that is fully developed with nonlinear mechanisms. Finally, BOUT++ simulations with a Braginskii fluid model highlight the importance of electron dynamics and equilibrium toroidal rotation for realistic pedestal turbulence simulations. Also, the BOUT++ simulations illustrate that simple, order-of-magnitude agreement between scalar turbulence quantities, such as correlation length, can be misleading when assessing the validity of simulations. The characterization and scalings of NSTX low-k pedestal turbulence and comparison to turbulence simulations provides an initial step towards validation of pedestal turbulence models in the challenging ST parameter regime.

Acknowledgments

The authors gratefully acknowledge helpful discussions with D.R. Mikkelsen and S.J. Zweben. This work was supported by US Department of Energy Grant Nos DE-FG02-89ER53296, DE-SC0001288 and DE-AC02-09CH11466.

References

[1] Groebner R.J. *et al* 2011 *Nucl. Fusion* **50** 064002
[2] Bongard M.W., Fonck R.J., Hegna C.C., Redd R.J. and Schlossberg D.J. 2011 *Phys. Rev. Lett.* **107** 035003
[3] Snyder P.B. *et al* 2009 *Phys. Plasmas* **16** 056118
[4] Peng Y.-K.M. 2000 *Phys. Plasmas* **7** 1681
[5] Snyder P.B., Wilson H.R., Osborne T.H. and Leonard A.W. 2004 *Plasma Phys. Control. Fusion* **46** A131
[6] Ono M. *et al* 2000 *Nucl. Fusion* **40** 557
[7] Kotschenreuther M., Dorland W., Liu Q.P., Zarnstorff M.C., Miller R.L. and Lin-Liu Y.R. 2000 *Nucl. Fusion* **40** 677
[8] Rewoldt G., Tang W.M., Kaye S. and Menard J. 1996 *Phys. Plasmas* **3** 1667
[9] Kaye S. *et al* 2007 *Nucl. Fusion* **47** 499
[10] Kaye S.M. *et al* 2007 *Phys. Rev. Lett.* **98** 175002
[11] Guttenfelder W. *et al* 2013 *Nucl. Fusion* **53** 093022
[12] Applegate D.J., Roach C.M., Connor J.W., Cowley S.C., Dorland W., Hastie R.J. and Joiner N. 2007 *Plasma Phys. Control. Fusion* **49** 1113
[13] Wong K.L., Kaye S., Mikkelsen D., Krommes J., Hill K., Bell R. and LeBlanc B. 2007 *Phys. Rev. Lett.* **99** 135003
[14] Wong K.L., Kaye S., Mikkelsen D.R., Krommes J.A., Hill K., Bell R. and LeBlanc B. 2008 *Phys. Plasmas* **15** 056108
[15] Guttenfelder W., Candy J., Kaye S.M., Nevins W.M., Wang E., Bell R.E., Hammett G.W., LeBlanc B.P., Mikkelsen D.R. and Yuh H. 2011 *Phys. Rev. Lett.* **106** 155004

[16] Guttenfelder W. *et al* 2012 *Phys. Plasmas* **19** 056119
[17] Diallo A., Kramer G.J., Smith D.R., Maingi R., Bell R.E., Guttenfelder W., LeBlanc B.P., Podesta M., McKee G.R. and Fonck R. 2013 *Phys. Plasmas* **20** 012505
[18] Canik J. *et al* 2012 *Proc. 2012 IAEA Fusion Energy Conf. (San Diego, CA, 8–13 October 2012)* www-pub.iaeameetings/41985/24th-Fusion-Energy-Conference
[19] Canik J.M. *et al* 2013 *Nucl. Fusion* **53** 113016
[20] Ghim Y.c. *et al* 2012 *Plasma Phys. Control. Fusion* **54** 095012
[21] Ghim Y.c. *et al* 2013 *Phys. Rev. Lett.* **110** 145002
[22] Smith D.R. *et al* 2013 *Phys. Plasmas* **20** 055903
[23] Yan Z., McKee G.R., Groebner R.J., Snyder P.B., Osborne T.H., Beurskens M.N. and Burrell K.H. 2011 *Phys. Plasmas* **18** 056117
[24] Kim C.C. and Parker S.E. 2000 *J. Comput. Phys.* **161** 589
[25] Chen Y. and Parker S.E. 2007 *J. Comput. Phys.* **220** 839
[26] Wan W., Parker S.E., Chen Y., Park G.-Y., Chang C.-S. and Stotler D. 2011 *Phys. Plasmas* **18** 056116
[27] Dudson B.D., Umansky M.V., Xu X.Q., Snyder P.B. and Wilson H.R. 2009 *Comput. Phys. Commun.* **180** 1467
[28] Umansky M.V., Xu X.Q., Dudson B.D., LoDestro L.L. and Myra J.R. 2009 *Comput. Phys. Commun.* **180** 887
[29] Smith D.R., Feder H., Feder R., Fonck R.J., Labik G., McKee G.R., Schoenbeck N., Stratton B.C., Uzun-Kaymak I. and Winz G. 2010 *Rev. Sci. Instrum.* **81** 10D717
[30] Smith D.R., Fonck R.J., McKee G.R. and Thompson D.S. 2012 *Rev. Sci. Instrum.* **83** 10D502
[31] Fonck R.J., Duperrex P.A., and Paul S.F. 1990 *Rev. Sci. Instrum.* **61** 3487
[32] Janev R.K., Boley C.D. and Post D.E. 1989 *Nucl. Fusion* **29** 2125
[33] Gianakon T.A., Fonck R.J., Callen J.D., Durst F.R. and Kim J.S. 1992 *Rev. Sci. Instrum.* **63** 4931
[34] LeBlanc B.P., Diallo A., Labik G. and Stevens D.R. 2012 *Rev. Sci. Instrum.* **83** 10D527
[35] Bell M. *et al* and the N.R. Team 2006 *Nucl. Fusion* **46** S565
[36] Bell R.E., Andre R., Kaye S.M., Kolesnikov R.A., LeBlanc B.P., Rewoldt G., Wang W.X. and Sabbagh S.A. 2010 *Phys. Plasmas* **17** 082507
[37] Field A.R., McCone J., Conway N.J., Dunstan M., Newton S. and Wisse M. 2009 *Plasma Phys. Control. Fusion* **51** 105002
[38] Kutner M., Nachtsheim C., Neter J. and Li W. 2004 *Applied Linear Statistical Models* 5th edn (New York: McGraw-Hill)
[39] Hjort N.L. and Claeskens G. 2003 *J. Am. Stat. Assoc.* **98** 879
[40] Bunea F., Tsybakov A.B., and Wegkamp M.H. 2007 *Ann. Stat.* **5** 1674
[41] Wan A.T.K., Zhang X. and Zou G. 2010 *J. Econometr.* **156** 277
[42] Magnus J.R., Powell O. and Prufer P. 2010 *J. Econometr.* **154** 139
[43] Hansen B.E. 2007 *Econometrica* **75** 1175
[44] Freckleton R.P. 2011 *Behav. Ecol. Sociobiol.* **65** 91
[45] Yeung K.Y., Bumgarner R.E. and Raftery A.E. 2005 *Bioinformatics* **21** 2394
[46] Lang J., Chen Y. and Parker S.E. 2007 *Phys. Plasmas* **14** 082315
[47] Peeters A.G., Angioni C., Apostoliceanu M., Jenko F. and Ryter F. 2005 *Phys. Plasmas* **12** 022505
[48] Snyder P.B. and Hammett G.W. 2001 *Phys. Plasmas* **8** 744
[49] Guttenfelder W., Candy J., Kaye S.M., Nevins W.M., Bell R.E., Hammett G.W., LeBlanc B.P. and Yuh H. 2012 *Phys. Plasmas* **19** 022506
[50] Kotschenreuther M., Dorland W., Beer M.A. and Hammett G.W. 1995 *Phys. Plasmas* **2** 2381
[51] Parra F.I., Barnes M., Highcock E.G., Schekochihin A.A. and Cowley S.C. 2011 *Phys. Rev. Lett.* **106** 115004
[52] Hahm T.S. and Burrell K.H. 1995 *Phys. Plasmas* **2** 1648
[53] Diamond P.H., Itoh S.-I., Itoh K. and Hahm T.S. 2005 *Plasma Phys. Control. Fusion* **47** R35
[54] Schekochihin A.A., Highcock E.G. and Cowley S.C. 2012 *Plasma Phys. Control. Fusion* **54** 055011
[55] Xu X. *et al* 2013 *Phys. Plasmas* **20** 056113